

ac Josephson effect in a gate-tunable Cd₃As₂ nanowire superconducting weak linkR. Haller^{1,*}, M. Osterwalder¹, G. Fülöp^{1,2}, J. Ridderbos^{1,3}, M. Jung⁴, and C. Schönenberger^{1,5,†}¹*Department of Physics, University of Basel, Klingelbergstrasse 82, CH-4056 Basel, Switzerland*²*Department of Physics, Institute of Physics, Budapest University of Technology and Economics and MTA-BME Nanoelectronics Momentum Research Group, Műegyetem rakpart 3, H-1111 Budapest, Hungary*³*MESA+ Institute for Nanotechnology, University of Twente, P.O. Box 217, 7500 AE Enschede, Netherlands*⁴*DGIST Research Institute, DGIST, Daegu 42988, Republic of Korea*⁵*Swiss Nanoscience Institute, University of Basel, Klingelbergstrasse 82, CH-4056 Basel, Switzerland* (Received 31 May 2023; revised 4 August 2023; accepted 22 August 2023; published 19 September 2023)

Three-dimensional topological Dirac semimetals have recently attracted significant attention since they possess exotic quantum states. When Josephson junctions are constructed utilizing these materials as the weak link, the fractional ac Josephson effect emerges in the presence of a topological supercurrent contribution. We investigate the ac Josephson effect in a Dirac semimetal Cd₃As₂ nanowire using two complementary methods: by probing the radiation spectrum and by measuring Shapiro patterns. With both techniques, we find that the conventional supercurrent dominates at all investigated doping levels and that any potentially present topological contribution falls below our detection threshold. The inclusion of thermal noise in a resistively and capacitively shunted junction (RCSJ) model allows us to reproduce the microwave characteristics of the junction. With this refinement, we explain how weak superconducting features can be masked and provide a framework to account for elevated electronic temperatures present in realistic experimental scenarios.

DOI: [10.1103/PhysRevB.108.094514](https://doi.org/10.1103/PhysRevB.108.094514)**I. INTRODUCTION**

Topological superconductivity is a hot topic in condensed matter physics since the quasiparticle excitations that govern its attributes, so-called Majorana fermions, follow non-Abelian exchange statistics—a property that could revolutionize quantum computation, as it allows the implementation of fault-tolerant operations [1–7]. While theoretical concepts on those exotic particles have already been developed in the past few decades [8–12], platforms to synthesize Majoranas are still being established, and clear experimental evidence of their existence is lacking [13].

We employ Dirac semimetal Cd₃As₂ nanowire Josephson junctions as a platform for the search for topological superconductivity. Dirac semimetals possess exotic electronic properties emerging from three-dimensional Dirac cones—crossings between valence and conduction bands with linear dispersion relations [14–19]. They host topological surface states [20] and develop Majorana flat bands in Josephson junctions [21]. Recently, the superconducting proximity effect was observed in Cd₃As₂ nanowires and nanoplates, including Josephson supercurrent carried by surface states [22]. In this context, π - and 4π -periodic supercurrent states and topological supercurrent oscillations have been reported [23,24].

In our Cd₃As₂ nanowire junctions, we hunt for signatures of the fractional ac Josephson effect arising from 4π -periodic contributions in the current-phase relation (CPR) that are a

direct consequence of topologically protected Andreev bound states, i.e., Majorana modes [8,25,26]. To this end, we investigate the ac Josephson effect by two complementary methods: (i) by the detection of Josephson radiation and (ii) by measuring Shapiro steps.

In the latter experiment, missing odd Shapiro steps are the fingerprint of topological supercurrent admixtures [27–29]. This effect has been observed for different material platforms: InSb nanowire junctions exposed to in-plane magnetic fields [30], Bi_xSe_y-based [31–33] and HgTe-based [34,35] topological insulator junctions, Bi_xSb_y Dirac semimetal nanoplate junctions [36], (Bi_{1-x}Sb_x)₂Te₃-based topological insulator nanowire junctions [37], and includes Cd₃As₂ nanowire junctions [24].

When measuring Josephson radiation, the signature of a topologically nontrivial supercurrent is the halving of the fundamental Josephson frequency $f_J = q^*V/h$, with q^* being the effective charge, V being the dc voltage bias, and h being the Planck constant. This occurs since the topological supercurrent is carried by single electrons ($q^* = e$) instead of Cooper pairs in the case of conventional junctions ($q^* = 2e$) [25,38]. Evidence for topological emission has been claimed only for a gate-tunable Al-HgTe-Al topological insulator junction [39] and for an Al-InAs-Al nanowire junction exposed to in-plane magnetic fields [40].

The (fractional) ac Josephson effect principally distinguishes conventional from topological junctions, but many experimental aspects pose a challenge to unambiguously prove the emergence of Majorana states, such as marginal 4π -supercurrent contributions, elevated electronic temperatures, environmental circuit effects [41,42], Landau-Zener

*roy.haller@unibas.ch

†<http://www.nanoelectronics.unibas.ch/>

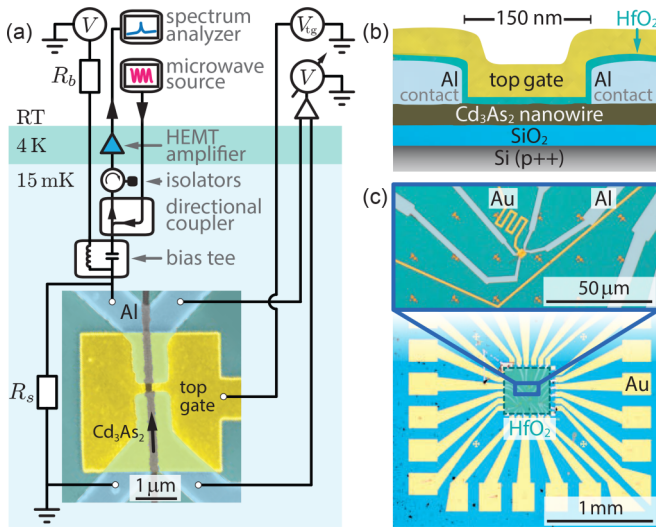


FIG. 1. Device and measurement setup. (a) Cd_3As_2 nanowire Josephson junction embedded in a radiation (irradiation) setup using a spectrum analyzer (microwave source). Inset: False-colored SEM image of the junction defined by superconducting Al leads (blue) in the Cd_3As_2 nanowire (center axis along the black arrow). The top gate electrode (yellow) is isolated from the junction by a 20 nm thick HfO_2 layer. The voltage V_{tg} applied on the Au gate allows tuning the charge carrier density. The junction is shunted by a resistor $R_s = 10 \Omega$ that connects the rf line to the fridge ground on the PCB. (b) Cross-sectional illustration of the junction along the black arrow in (a). (c) Optical image showing the electrodes extending from the junction (top) towards the Au bonding pads shown on the overview of the chip (bottom).

transitions [43–46], hardly tunable junctions parameters [47–49], lifetime broadening, and a finite detection bandwidth [47,50]. The approach to combine Shapiro measurements with radiation measurements on a single Josephson junction, as in Ref. [51], should greatly reduce ambiguity about its topological nature. Furthermore, the fractional radiation signal can be detected independent of the magnitude of the trivial supercurrent. This is in contrast to Shapiro step measurements, where the ratio of the topological to trivial supercurrent mainly determines its resolvability [24].

In this work, we investigate a gate-tunable Cd_3As_2 nanowire Josephson junction by assessing the dc and ac Josephson effects. By including thermal fluctuations in the resistively and capacitively shunted junction (RCSJ) model, we successfully reproduce the obtained I V curves, Josephson emission spectra, and Shapiro patterns using only a conventional, sinusoidal 2π -periodic CPR. The comparison enables us to determine the effective electron temperature of the system, which, in turn, imposes limitations on the sensitivity and may serve as a possible explanation for the absence of fractional signatures in the ac Josephson effect.

II. DEVICE AND MEASUREMENT SETUP

Figure 1(a) shows the Cd_3As_2 nanowire Josephson junction device and the schematic of the measurement setup. The nanowires were grown on a separate chip using the vapor transport method [20,22,52–55], which is detailed in

the Supplemental Material (SM) in Sec. SII [56]. With a clean room wipe snippet they are transferred onto a highly p doped Si/SiO_2 (500 $\mu\text{m}/305 \text{ nm}$) wafer with prepatterned Au markers and bonding pads. After removing the native oxide of the nanowire with Ar milling, the wire is *in situ* contacted by Ti/Al (3 nm/200 nm) electrodes in a quasi-four-probe configuration. The Al leads turn superconducting below a critical temperature $T_c \approx 1.2 \text{ K}$ and extend from the nanowire up to the inner border of the base structures. The nanowire presented here has a diameter of 50 nm and a junction length of 150 nm, determined by the contact spacing. A cross-sectional cut through the device structure, parallel to the nanowire, is illustrated in Fig. 1(b). A locally deposited layer of HfO_2 (20 nm) covering the whole inner part of the chip [see Fig. 1(c)] serves as gate dielectric for the Au top gate, which allows tuning the charge carrier density inside the wire by applying a gate voltage V_{tg} .

The measurement setup shown in Fig. 1(a) allows probing the ac Josephson effect in two ways. First, the Josephson radiation emitted from the junction under finite dc bias can be detected directly with a spectrum analyzer. Second, the reverse experiment can be done: irradiating the device with an ac field emitted by a microwave source while measuring the dc transport response of the junction, resulting in Shapiro steps [57]. In this case, a directional coupler feeds the incoming microwave tone to the sample, whereas in the Josephson radiation experiment, it directs the signal emitted by the junction to the spectrum analyzer. The outgoing signal passes through isolator stages, limiting the detection bandwidth to 2.5–3.8 GHz, after which the signal gets amplified by a high-electron-mobility transistor (HEMT).

Our dc setup sources a current using a bias resistor $R_b = 1 \text{ M}\Omega$ in series with a dc voltage source with a small ac component with frequency $f = 177 \text{ Hz}$ supplied by a lock-in amplifier. This current is applied via a bias tee to the microwave line that directly connects to the source of the sample. The other side of the sample is galvanically connected to ground, closing both the low- and high-frequency circuits. When the sample is in the nonsuperconducting regime, the signal is converted to a stable voltage bias by shunting the device with a resistor $R_s = 10 \Omega$. This shunt resistor is directly placed between the central conductor of the transmission line and the galvanic ground on the sample holder. We measure the differential resistance of the shunted device using a voltage amplifier and lock-in techniques. All measurements are performed in a dilution refrigerator hosting filtered dc lines [58] with a base temperature of $\sim 15 \text{ mK}$. Details of the measurement setup and the device integration on the printed circuit board (PCB) are given in Sec. SIII in the SM [56].

III. MEASUREMENT RESULTS

We first probe the gate-dependent dc response of the junction, which is presented in Fig. 2. The differential resistance as a function of current I bias and top gate voltage V_{tg} in Fig. 2(a) reveals a clear switching behavior from a zero-resistance superconducting state (black) to a normal resistive state (blue). We attribute the peaks in differential resistance to the critical current I_c , which become sharper and more pronounced for higher I_c , as seen in Fig. 2(b). Under sufficiently large current

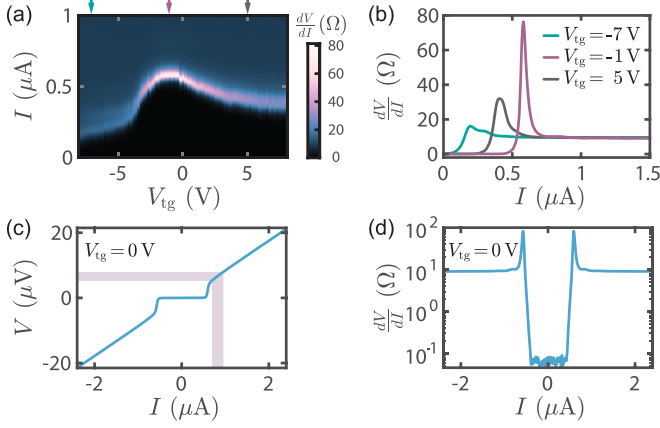


FIG. 2. Gate-dependent supercurrent. (a) Differential resistance dV/dI as a function of current bias I and top gate voltage V_{tg} . (b) dV/dI as a function of I at different gate voltages taken from the line cut in (a) at the positions indicated by the arrows. The dV/dI -peak position is identified as the critical current I_c . (c) IV characteristic at $V_{tg} = 0$ V obtained by integrating the measured dV/dI shown in logarithmic scale in (d). The violet shaded area indicates the current and voltage range that produces conventional Josephson radiation in a 2.5–3.8 GHz bandwidth.

bias the differential resistance approaches R_s . As a function of V_{tg} , we observe an anomalous evolution of I_c ; when we sweep the gate from negative to positive voltages, I_c first increases and then decreases again in an asymmetric way with a maximum of $I_c = 580$ nA at $V_{tg} = -1$ V. This behavior is in contrast to that of ordinary semiconductor Josephson junctions, which generally exhibit a steady increase in the critical current as a function of larger electric-field-induced doping. The unusual gate response was previously reported in long Cd_3As_2 nanowire Josephson junctions and was proposed to originate from scattering mechanisms between surface and bulk states that give rise to dephasing [22]. In this case, one assumes the majority of the supercurrent is carried by surface states and increasing the electron density enhances scattering with bulk modes, which, in turn, results in a suppression of the coherent Cooper pair transport and hence leads to a reduction in I_c . This hypothesis is further supported by the $I_c R_N$ product discussed in Sec. SV in the SM [56].

In Fig. 2(c), the IV curve at $V_{tg} = 0$ V, obtained by integrating the measured dV/dI curve presented in Fig. 2(d), shows a clear voltage plateau which we assume is zero. In the normal state, the junction shows Ohmic behavior down to $5 \mu\text{V}$, which allows steady voltage biasing in the regime of conventional Josephson radiation for the given detection bandwidth (violet shading).

In the next step, we investigate the Josephson radiation spectrum at $V_{tg} = 0$ V, for which $I_c = 570$ nA. In Fig. 3(a), the normalized power spectral density collected for a 20 MHz bandwidth is plotted as a function of voltage bias V and detection frequency f_{det} . The normalization for each f_{det} allows us to compensate for the frequency-dependent background. The detected radiation features are symmetric in voltage and solely determined by conventional Josephson emission arising due to the inelastic transfer of Cooper pairs. The signal follows the fundamental ac Josephson relation $V = hf_J/(2e)$,

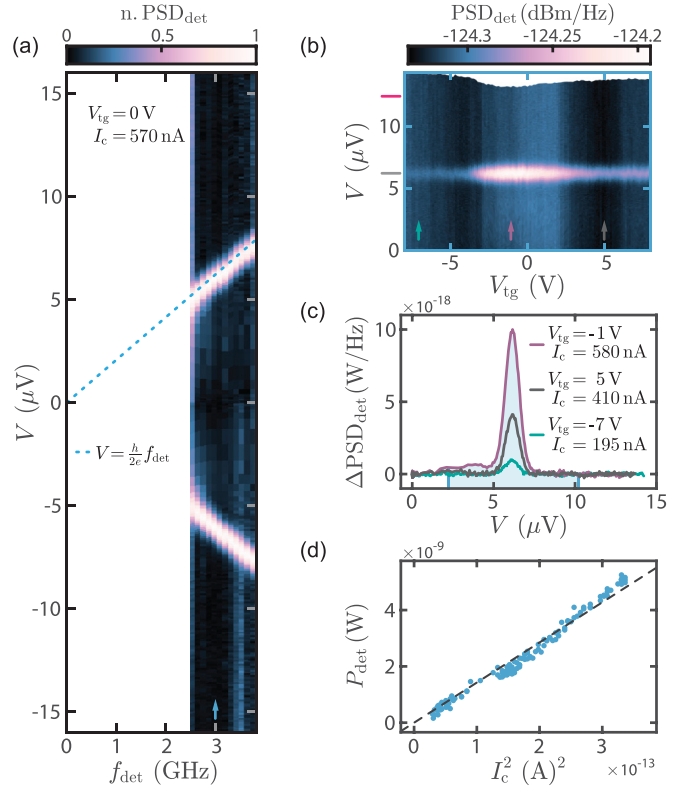


FIG. 3. Emission spectrum. (a) Normalized power spectral density (n. PSD_{det}) as a function of the voltage drop V across the junction and detection frequencies f_{det} at $V_{tg} = 0$ V. The radiation spectrum is overlaid with the expected peak position of conventional Josephson emission. (b) Power spectral density (PSD_{det}) as a function of V and V_{tg} , measured at a fixed detection frequency $f_{det} = 3$ GHz indicated by the blue arrow in (a). The gray mark on the voltage axis indicates the expected conventional emission peak position, whereas the pink mark is placed at the position of a potential topologically nontrivial emission peak. (c) PSD_{det} in linear scale with a subtracted background (ΔPSD_{det}) as a function of V at three gate voltages obtained from line cuts in (b) at the positions indicated by the arrows. (d) Emission strength P_{det} (W) plotted against the corresponding critical current squared I_c^2 .

illustrated by the dashed line. When the detection frequency of the spectrum analyzer is aligned with the Josephson frequency ($f_J = f_{det}$), the power spectral density peaks. Neither signatures from topological supercurrent contributions that would evolve as $V = hf_J/e$ nor clear higher-order emission features are observed. The latter is expected for a Josephson junction possessing a CPR consisting of $\sin(n\varphi)$ harmonics, with $n = 2, 3, 4, \dots$, i.e., a skewed CPR in which multiple Cooper pairs counted by n are involved in one effective transfer event [59–63], resulting in higher-order emission peaks following the relation $V = hf_J/(n2e)$. Therefore, we conclude that our junction dynamics are dominated by a sinusoidal 2π -periodic CPR.

Next, we look for the emergence of a topological phase as a function of doping level in Fig. 3(b), where we measured the power spectral density with fixed $f_{det} = 3$ GHz while sweeping V across the junction for different V_{tg} . We note the voltage position for topologically nontrivial emission ($V = hf_J/e$) in

pink, at which no additional radiation peaks appear. The conventional emission peak modulates in intensity but remains visible throughout the whole gate range and aligns with the conventional voltage position ($V = hf_j/2e$) marked in gray.

To estimate a lower bound of the sensitivity in terms of I_c , we relate the emission strength to the critical current. We first convert the raw data from dBm/Hz scale to W/Hz scale and subtract for each gate voltage a linear background such that regions far away from the radiation peaks have vanishingly small contributions. The so-obtained relative emission density ($\Delta\text{PSD}_{\text{det}}$) as a function of V is shown in Fig. 3(c) for different V_{tg} , corresponding to different I_c that are extracted from Fig. 2(a). In Fig. 3(d) we correlate the emission strength P_{det} to the square of the critical current I_c^2 . P_{det} is obtained by integrating $\Delta\text{PSD}_{\text{det}}$ over the voltage interval (2.2–10.2 μV) that is indicated with the light blue shading in Fig. 3(c) as $P_{\text{det}}(\text{W}) = \frac{2e}{h} \int_{2.2\mu\text{V}}^{10.2\mu\text{V}} \Delta\text{PSD}_{\text{det}} [\text{W/Hz}] dV$. These integration bounds certainly embrace the interval of enhanced emission. We recognize a clear quadratic dependence between P_{det} and I_c . Considering the junction as a sinusoidal ac current source with amplitude I_c , indeed, a power $P_{\text{det}} = \mathcal{R}I_c^2/2$ is dissipated in the detector, where \mathcal{R} describes the power transfer ratio, detailed in the SM in Sec. SIV [56]. From the power to critical current relation, we estimate, for the given experimental configuration and under the assumption of a sinusoidal 2π -periodic CPR, a lower detection limit of $I_c \approx 55$ nA. This is a potential explanation for the lack of topological signatures in the radiation spectrum since it is known that the associated nontrivial supercurrent in Cd_3As_2 nanowires may be only a small fraction ($\leq 10\%$) of the overall critical current [24]. Importantly, even small topological current fractions ($\leq 50\%$) can give radiation spectra with predominantly topological features [28,39], in which case the topological detection limit amplitude can be significantly lower than the trivial one. However, we find from our model (see the SM, Sec. SI [56]) that for detection frequencies where both the trivial and topological signals are generated in the linear response regime, i.e., in the Ohmic branch of the IV curve, the individual emission strengths correspond to first order to the underlying current amplitudes, a situation that also applies to our investigated device [see Fig. 2(c)]. We therefore conclude that our detection limit is a safe upper bound for both the trivial and topological supercurrents.

We now expand the investigation of the ac Josephson effect by measuring the Shapiro step pattern. Here, the junction is irradiated by a microwave tone of fixed frequency $f_d = 2$ GHz at variable output power P_s of the signal generator. We probe the differential resistance dV/dI as a function of current bias I and P_s for a constant gate voltage $V_{\text{tg}} = 0$ V. The resulting map, shown in Fig. 4(a), reveals the characteristic voltage plateaus in regions of vanishing dV/dI (dark teardrop shapes). With increasing P_s , the 0th plateau ($V = 0$) diminishes, while higher-order Shapiro steps progressively emerge. In Fig. 4(b) we present the IV curve obtained by integrating dV/dI for different drive powers, and the voltage axis in units of the Shapiro voltage matches the measured voltage steps. By numerically differentiating the interpolated IV curves we can extract the differential conductance dI/dV , which is presented in Fig. 4(c) as a function of V and P_s for different

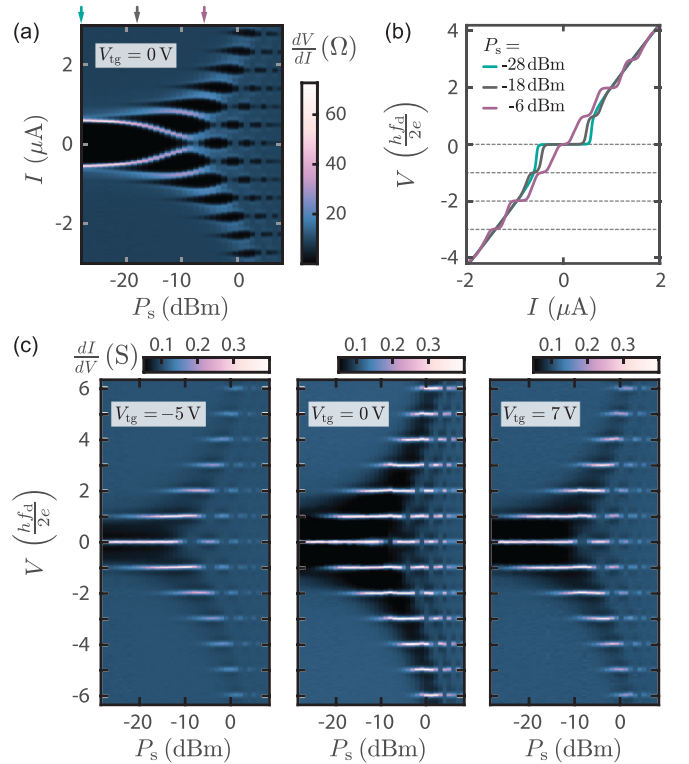


FIG. 4. Shapiro step measurement with drive frequency $f_d = 2$ GHz. (a) Differential resistance dV/dI as a function of drive power P_s at the microwave source and current bias I . (b) IV curves obtained by integrating dV/dI for irradiation powers indicated by the arrows in (a), with the voltage axis normalized to the Shapiro step voltage $hf_d/2e$. (c) Differential conductance dI/dV as a function of P_s and V in units of the Shapiro step voltage $hf_d/2e$, measured on the hole side ($V_{\text{tg}} = -5$ V), the electron side ($V_{\text{tg}} = 7$ V), and close to the Dirac point ($V_{\text{tg}} = 0$ V). Data are numerically converted from current-biased data; the center map constitutes the same measurement as in (a).

top gate voltages. With this visualization technique, no binning is required, and the resolution is maintained [64]. The voltage plateaus appear as lines in the color map, whereas their intensities reflect the width of the Shapiro steps. In agreement with the lack of topological signatures in the radiation measurement, no modulation in the width of subsequent steps is observed in the experimentally accessed parameter space, as evaluated in Sec. SVI in the SM [56].

IV. RCSJ SIMULATION WITH THERMAL FLUCTUATIONS

To gain a deeper understanding of the junction dynamics, we aim to reproduce our experimental results in the framework of the RCSJ model. To be able to reproduce our experimental data, we include a noise term to account for thermal fluctuations [65]. Consequently, the model [66], which is detailed in the SM in Sec. SI [56], contains the following parameters: the critical current I_c , the shunt resistance R , the shunt capacitance C , and the effective temperature T . Furthermore, the shape of the CPR matters, which in the following is set to a sinusoidal, 2π -periodic function $I_s = I_c \sin(\varphi)$, where φ represents the phase drop and I_s is the supercurrent across

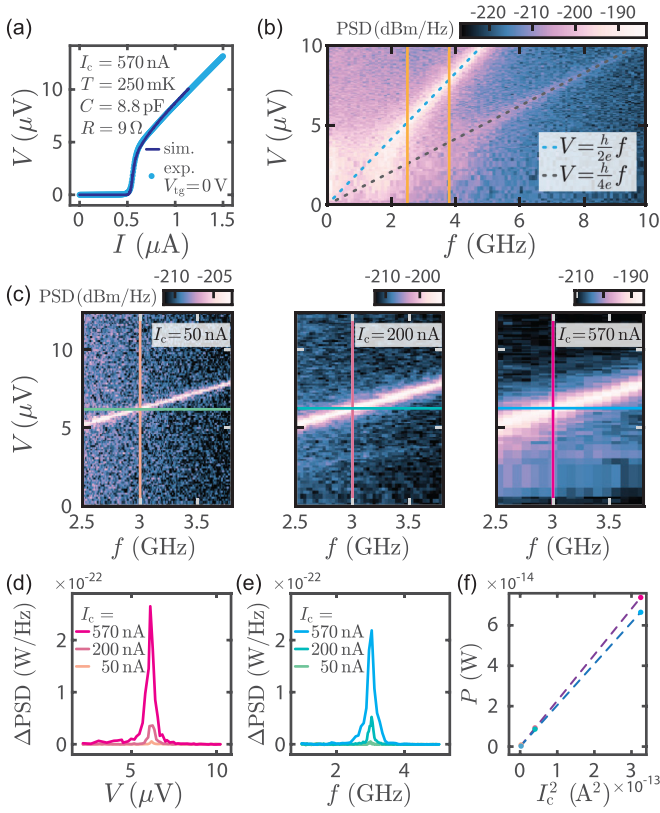


FIG. 5. Results of RCSJ modeling with thermal fluctuations. (a) Simulated IV characteristics (dark blue) fitted to the experimental curve at $V_g = 0$ V (light blue). The fit parameters critical current I_c , effective temperature T , shunt capacitance C , and shunt resistance R are listed. T , C , and R are kept constant for the subsequent plots. (b) Simulated power spectral density (PSD) as a function of mean voltage V and frequency f deduced from the voltage evolution in time for $I_c = 570$ nA. The map is overlaid with the fundamental (blue) voltage-to-frequency conversion and the first higher harmonic (gray). The orange vertical lines indicate the frequency range (2.5–3.8 GHz) of interest for the comparison with the experiment. (c) Simulated emission spectrum for different I_c . (d) and (e) PSD in linear scale with a subtracted background (ΔPSD) for different I_c deduced from the maps presented in (c) for a given frequency and voltage, respectively. In (d) $f = 3$ GHz, and in (e) its voltage equivalent $V = 6.2$ μV , which is related to vertical and horizontal cuts presented in (c). (f) Emission strength P plotted against the corresponding critical current squared I_c^2 by integrating over the voltage (P_V ; purple) and by integrating over the frequency (P_f ; blue).

the junction. The discussion is extended to admixtures of 2π - and 4π -periodic CPRs in Sec. SI in the SM [56].

The output of the model is the time evolution of the junction phase $\varphi(t)$, from which the junction voltage is calculated using the ac Josephson relation, $V(t) = \frac{\hbar}{2e} \frac{d\varphi(t)}{dt}$, with $\hbar = h/2\pi$. First, we consider the time-averaged results of the modified RCSJ model to fit the experimentally obtained IV curve at $V_g = 0$ V as presented in Fig. 5(a). With the obtained model parameters that are listed in the plot, the junction quality factor $Q = \sqrt{2eI_c}/(\hbar C)RC \approx 1$ is obtained, which classifies the junction into the intermediately damped regime [67], which is further supported by the smooth

switching behavior accompanied by a tiny hysteresis of ~ 10 nA between up and down current bias sweeps (not shown). The elevated effective temperature ($T = 250$ mK) with respect to the base temperature ($T_b = 15$ mK) originates from external noise, likely generated by the HEMT configured at a suboptimal operating point, an issue that was only later identified.

In the next step, we employ the extracted parameters and focus on the time-dependent $V(t)$ solutions of the RCSJ model to reproduce the emission spectrum. By taking the squared magnitude of the Fourier transform of $V(t)$, we calculate the voltage noise spectral density as a function of frequency f [68] and convert it to power spectral density (PSD). Here, we do not include any amplification of the signal; the comparison of absolute signal levels between the experiment and simulation is discussed in the SM in Sec. SIV [56]. In Fig. 5(b) we plot the simulated PSD as a function of f and averaged voltage V . Within the experimentally accessible range, indicated by the orange lines, the simulation qualitatively reproduces the detected emission spectrum previously presented in Fig. 3(a). Interestingly, the simulation reveals, in addition to the conventional voltage to frequency relation (blue dashed line), an emission peak at double the frequency for a given voltage (gray dashed line). We attribute this feature to the current bias in our model, leading to higher-order modes of frequency $f = n2eV/h$ [62]. In this manner, higher-order features can be generated from a purely sinusoidal CPR, as seen in the simulations for different model parameters presented in Sec. SI in the SM [56].

We now direct our attention to the modeled emission strength as a function of I_c . Figure 5(c) shows simulated radiation maps for increasing I_c , with f corresponding to our experimental range. For each I_c we generate voltage linecuts for fixed $f = 3$ GHz (orange, pink, and magenta lines) and extract the corresponding frequency linecuts for fixed $V = 6.2$ μV (green, aqua, and blue lines). In Figs. 5(d) and 5(e) we evaluate ΔPSD by subtracting a linear background for the voltage cuts and a $1/f$ background for the frequency cuts, from which we obtain the emission strength of the junction: (i) by integrating ΔPSD over the voltage interval 2.2–10.2 μV as $P_V(\text{W}) = \frac{2e}{h} \int_{2.2\mu\text{V}}^{10.2\mu\text{V}} \Delta\text{PSD} [\text{W}/\text{Hz}] dV$ and (ii) by integrating ΔPSD over the voltage corresponding frequency interval 1–5 GHz as $P_f(\text{W}) = \int_{1\text{GHz}}^{5\text{GHz}} \Delta\text{PSD} [\text{W}/\text{Hz}] df$. The thus obtained emission strength is linearly correlated to I_c^2 , as illustrated in Fig. 5(f), where the procedure via integration over the voltage (frequency) is shown in purple (blue). We attributed the slightly enhanced emission strength obtained from the voltage integration procedure to higher-order contributions appearing at integer fractions of the main emission peak.

By adding an ac current bias excitation in the RCSJ model expressed in drive power P_d at the device, it is also capable of generating Shapiro step patterns. Employing the same model parameters as before, we find good agreement in the Shapiro pattern between the simulation presented in Fig. 6 and the experiment shown in Fig. 4, again by using a 2π -periodic sinusoidal CPR. In Sec. SVI in the SM [56] we analyze simulated Shapiro step patterns with CPRs containing an admixture of topologically nontrivial $\sin(\varphi/2)$ CPR

contributions. In contrast to the evaluation of the radiation experiment, where an absolute detection limit can be defined, with the step width analysis a relative detection threshold can be established. For the specific parameters used, we find that below a topological to conventional CPR ratio of $\sim 10\%$, the topological features are masked by the dominating 2π -periodic supercurrent.

V. CONCLUSION

We investigated the dc and ac Josephson effects in a single Cd_3As_2 nanowire Josephson junction. Although we observed an anomalous evolution of the critical current as a function of gate voltage that points to the presence of supercurrent-carrying surface states, no direct evidence of topological superconductivity was found in either the Josephson radiation measurement or the Shapiro pattern evaluation. Importantly, we reproduced our experimental findings using a refined RCSJ model that includes thermal fluctuations, and we obtained an effective electronic temperature $T \approx 250$ mK which masks emission signals from supercurrents < 55 nA, highlighting the importance of reducing thermal noise.

The work on $(\text{Bi}_{1-x}\text{Sb}_x)_2\text{Te}_3$ [51] similarly found no evidence of the fractional Josephson effect, which the authors attributed to a large shunt capacitance that reduced the power reaching their detector. We face similar detection limit challenges which could be overcome by improving the filtering, minimizing the ground noise, matching the junction and detector impedance, optimizing the detector settings, and adding a Josephson parametric amplifier to the amplification chain. The resulting gain in the signal-to-noise ratio will hopefully allow us to resolve much lower supercurrents and reveal the topological nature of these materials.

All raw and metadata in this paper are available in numerical form together with the processing codes from Zenodo [69].

ACKNOWLEDGMENTS

We are grateful for scientific discussions with C. Li. This research was supported by the Swiss National Science Foundation through (a) Grants No. 172638 and No. 192027, (b) the

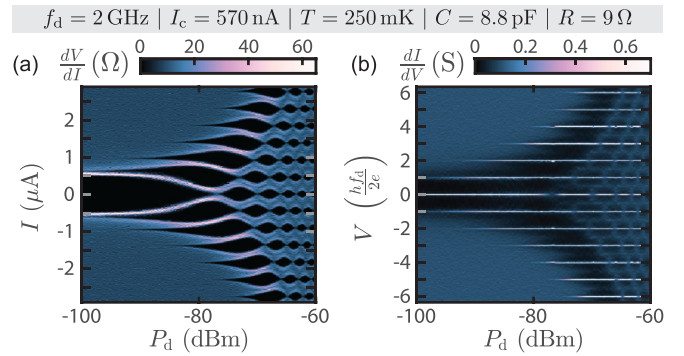


FIG. 6. Simulated Shapiro pattern reproducing the experimentally obtained features at $V_{\text{ig}} = 0$ V presented in Fig. 4. The parameters used in the RCSJ model with thermal fluctuations are listed. (a) Differential resistance dV/dI as a function of drive power P_d at the device and current bias I . (b) Differential conductance dI/dV as a function of P_d and V in units of the Shapiro step voltage $hf_d/2e$.

National Centre of Competence in Research Quantum Science and Technology (QSIT), and (c) the QuantEra project Super-Top; the János Bolyai Research Scholarship of the Hungarian Academy of Sciences; the National Research Development and Innovation Office (NKFIH) through OTKA Grants No. FK 132146 and No. NN127903 (FlagERA Topograph); the National Research, Development and Innovation Fund of Hungary within the Quantum Technology National Excellence Program (Project No. 2017-1.2.1-NKP-2017-00001); the Quantum Information National Laboratory of Hungary; and the ÉNKP-22-5 New National Excellence Program. We further acknowledge funding from the European Union's Horizon 2020 research and innovation program, specifically from (a) European Research Council (ERC) Grant Agreement No. 787414, ERC-Adv TopSupra, (b) Grant Agreement No. 862046, FET TOPSQUAD, and (c) Grant Agreement No. 828948, FET-open project AndQC. M.J. is supported by the midcareer research program (NRF-2023R1A2C1004832) through the National Research Foundation of Korea (NRF) grant.

- [1] A. Y. Kitaev, *Phys. Usp.* **44**, 131 (2001).
- [2] A. Kitaev, *Ann. Phys. (NY)* **303**, 2 (2003).
- [3] D. A. Ivanov, *Phys. Rev. Lett.* **86**, 268 (2001).
- [4] C. Nayak, S. H. Simon, A. Stern, M. Freedman, and S. D. Sarma, *Rev. Mod. Phys.* **80**, 1083 (2008).
- [5] F. Wilczek, *Nat. Phys.* **5**, 614 (2009).
- [6] A. Stern and N. H. Lindner, *Science* **339**, 1179 (2013).
- [7] T. Karzig, C. Knapp, R. M. Lutchyn, P. Bonderson, M. B. Hastings, C. Nayak, J. Alicea, K. Flensberg, S. Plugge, Y. Oreg, C. M. Marcus, and M. H. Freedman, *Phys. Rev. B* **95**, 235305 (2017).
- [8] L. Fu and C. L. Kane, *Phys. Rev. B* **79**, 161408(R) (2009).
- [9] R. M. Lutchyn, J. D. Sau, and S. D. Sarma, *Phys. Rev. Lett.* **105**, 077001 (2010).
- [10] J. D. Sau, R. M. Lutchyn, S. Tewari, and S. Das Sarma, *Phys. Rev. Lett.* **104**, 040502 (2010).
- [11] J. Alicea, *Phys. Rev. B* **81**, 125318 (2010).
- [12] X. L. Qi and S. C. Zhang, *Rev. Mod. Phys.* **83**, 1057 (2011).
- [13] S. M. Frolov, M. J. Manfra, and J. D. Sau, *Nat. Phys.* **16**, 718 (2020).
- [14] S. M. Young, S. Zaheer, J. C. Y. Teo, C. L. Kane, E. J. Mele, and A. M. Rappe, *Phys. Rev. Lett.* **108**, 140405 (2012).

- [15] Z. Wang, Y. Sun, X.-Q. Chen, C. Franchini, G. Xu, H. Weng, X. Dai, and Z. Fang, *Phys. Rev. B* **85**, 195320 (2012).
- [16] Z. Wang, H. Weng, Q. Wu, X. Dai, and Z. Fang, *Phys. Rev. B* **88**, 125427 (2013).
- [17] A. Burkov, *Nat. Mater.* **15**, 1145 (2016).
- [18] N. P. Armitage, E. J. Mele, and A. Vishwanath, *Rev. Mod. Phys.* **90**, 015001 (2018).
- [19] I. Crassee, R. Sankar, W.-L. Lee, A. Akrap, and M. Orlita, *Phys. Rev. Mater.* **2**, 120302 (2018).
- [20] S. Jeon, B. B. Zhou, A. Gyenis, B. E. Feldman, I. Kimchi, A. C. Potter, Q. D. Gibson, R. J. Cava, A. Vishwanath, and A. Yazdani, *Nat. Mater.* **13**, 851 (2014).
- [21] A. Chen, D. I. Pikulin, and M. Franz, *Phys. Rev. B* **95**, 174505 (2017).
- [22] C.-Z. Li, C. Li, L.-X. Wang, S. Wang, Z.-M. Liao, A. Brinkman, and D.-P. Yu, *Phys. Rev. B* **97**, 115446 (2018).
- [23] W. Yu, W. Pan, D. L. Medlin, M. A. Rodriguez, S. R. Lee, Z.-Q. Bao, and F. Zhang, *Phys. Rev. Lett.* **120**, 177704 (2018).
- [24] A.-Q. Wang, C.-Z. Li, C. Li, Z.-M. Liao, A. Brinkman, and D.-P. Yu, *Phys. Rev. Lett.* **121**, 237701 (2018).
- [25] D. M. Badiane, L. I. Glazman, M. Houzet, and J. S. Meyer, *C. R. Phys.* **14**, 840 (2013).
- [26] J.-J. Feng, Z. Huang, Z. Wang, and Q. Niu, *Phys. Rev. B* **101**, 180504(R) (2020).
- [27] F. Domínguez, F. Hassler, and G. Platero, *Phys. Rev. B* **86**, 140503(R) (2012).
- [28] F. Domínguez, O. Kashuba, E. Bocquillon, J. Wiedenmann, R. S. Deacon, T. M. Klapwijk, G. Platero, L. W. Molenkamp, B. Trauzettel, and E. M. Hankiewicz, *Phys. Rev. B* **95**, 195430 (2017).
- [29] J. Picó-Cortés, F. Domínguez, and G. Platero, *Phys. Rev. B* **96**, 125438 (2017).
- [30] L. P. Rokhinson, X. Liu, and J. K. Furdyna, *Nat. Phys.* **8**, 795 (2012).
- [31] K. Le Calvez, L. Veyrat, F. Gay, P. Plaidoux, C. B. Winkelmann, H. Courtois, and B. Saccépé, *Commun. Phys.* **2**, 4 (2019).
- [32] P. Schüffelgen, D. Rosenbach, C. Li, T. W. Schmitt, M. Schlenvoigt, A. R. Jalil, S. Schmitt, J. Kölzer, M. Wang, B. Bennemann, U. Parlak, L. Kibkalo, S. Trelenkamp, T. Grap, D. Meertens, M. Luysberg, G. Mussler, E. Berenschot, N. Tas, A. A. Golubov, A. Brinkman, T. Schäpers, and D. Grützmacher, *Nat. Nanotechnol.* **14**, 825 (2019).
- [33] R. Yano, M. Koyanagi, H. Kashiwaya, K. Tsumura, H. T. Hirose, Y. Asano, T. Sasagawa, and S. Kashiwaya, *J. Phys. Soc. Jpn.* **89**, 034702 (2020).
- [34] J. Wiedenmann, E. Bocquillon, R. S. Deacon, S. Hartinger, O. Herrmann, T. M. Klapwijk, L. Maier, C. Ames, C. Brüne, C. Gould, A. Oiwa, K. Ishibashi, S. Tarucha, H. Buhmann, and L. W. Molenkamp, *Nat. Commun.* **7**, 10303 (2016).
- [35] E. Bocquillon, R. S. Deacon, J. Wiedenmann, P. Leubner, T. M. Klapwijk, C. Brüne, K. Ishibashi, H. Buhmann, and L. W. Molenkamp, *Nat. Nanotechnol.* **12**, 137 (2017).
- [36] C. Li, J. C. de Boer, B. de Ronde, S. V. Ramankutty, E. van Heumen, Y. Huang, A. de Visser, A. A. Golubov, M. S. Golden, and A. Brinkman, *Nat. Mater.* **17**, 875 (2018).
- [37] M. Bai, X.-K. Wei, J. Feng, M. Luysberg, A. Bliesener, G. Lippertz, A. Uday, A. A. Taskin, J. Mayer, and Y. Ando, *Commun. Mater.* **3**, 20 (2022).
- [38] H.-J. Kwon, K. Sengupta, and V. M. Yakovenko, *Eur. Phys. J. B* **37**, 349 (2003).
- [39] R. S. Deacon, J. Wiedenmann, E. Bocquillon, F. Domínguez, T. M. Klapwijk, P. Leubner, C. Brüne, E. M. Hankiewicz, S. Tarucha, K. Ishibashi, H. Buhmann, and L. W. Molenkamp, *Phys. Rev. X* **7**, 021011 (2017).
- [40] D. Laroche, D. Bouman, D. J. van Woerkom, A. Proutski, C. Murthy, D. I. Pikulin, C. Nayak, R. J. J. van Gulik, J. Nygård, P. Krogstrup, L. P. Kouwenhoven, and A. Geresdi, *Nat. Commun.* **10**, 245 (2019).
- [41] H. Kamata, R. S. Deacon, S. Matsuo, K. Li, S. Jeppesen, L. Samuelson, H. Q. Xu, K. Ishibashi, and S. Tarucha, *Phys. Rev. B* **98**, 041302(R) (2018).
- [42] S. R. Mudi and S. M. Frolov, *arXiv:2106.00495*.
- [43] P.-M. Billangeon, F. Pierre, H. Bouchiat, and R. Deblock, *Phys. Rev. Lett.* **98**, 216802 (2007).
- [44] M. C. Dartiailh, J. J. Cuozzo, B. H. Elfeky, W. Mayer, J. Yuan, K. S. Wickramasinghe, E. Rossi, and J. Shabani, *Nat. Commun.* **12**, 78 (2021).
- [45] I. T. Rosen, C. J. Trimble, M. P. Andersen, E. Mikheev, Y. Li, Y. Liu, L. Tai, P. Zhang, K. L. Wang, Y. Cui, M. A. Kastner, J. R. Williams, and D. Goldhaber-Gordon, *arXiv:2110.01039*.
- [46] B. H. Elfeky, J. J. Cuozzo, N. Lotfizadeh, W. F. Schiela, S. M. Farzaneh, W. M. Strickland, D. Langone, E. Rossi, and J. Shabani, *ACS Nano* **17**, 4650 (2023).
- [47] M. Houzet, J. S. Meyer, D. M. Badiane, and L. I. Glazman, *Phys. Rev. Lett.* **111**, 046401 (2013).
- [48] J. Park, Y.-B. Choi, G.-H. Lee, and H.-J. Lee, *Phys. Rev. B* **103**, 235428 (2021).
- [49] Y. Jang and Y.-J. Doh, *J. Korean Phys. Soc.* **78**, 58 (2021).
- [50] P. San-Jose, E. Prada, and R. Aguado, *Phys. Rev. Lett.* **108**, 257001 (2012).
- [51] Y. Takeshige, S. Matsuo, R. S. Deacon, K. Ueda, Y. Sato, Y. F. Zhao, L. Zhou, C. Z. Chang, K. Ishibashi, and S. Tarucha, *Phys. Rev. B* **101**, 115410 (2020).
- [52] M. Jung, K. Yoshida, K. Park, X.-X. Zhang, C. Yesilyurt, Z. B. Siu, M. B. A. Jalil, J. Park, J. Park, N. Nagaosa, J. Seo, and K. Hirakawa, *Nano Lett.* **18**, 1863 (2018).
- [53] K. Park, M. Jung, D. Kim, J. R. Bayogan, J. H. Lee, S. J. An, J. Seo, J. Seo, J.-P. Ahn, and J. Park, *Nano Lett.* **20**, 4939 (2020).
- [54] C.-Z. Li, L.-X. Wang, H. Liu, J. Wang, Z.-M. Liao, and D.-P. Yu, *Nat. Commun.* **6**, 10137 (2015).
- [55] E. Zhang, Y. Liu, W. Wang, C. Zhang, P. Zhou, Z.-G. Chen, J. Zou, and F. Xiu, *ACS Nano* **9**, 8843 (2015).
- [56] See Supplemental Material at <http://link.aps.org/supplemental/10.1103/PhysRevB.108.094514> for details about the RCSJ model (Sec. SI), nanowire growth (Sec. SII) and measurement setup (Sec. SIII), valuation of the Josephson emission power (Sec. SIV) and $I_c R_N$ product (Sec. SV), and the evaluation of Shapiro patterns (Sec. SVI).
- [57] S. Shapiro, *Phys. Rev. Lett.* **11**, 80 (1963).
- [58] C. P. Scheller, S. Heizmann, K. Bedner, D. Giss, M. Meschke, D. M. Zumbühl, J. D. Zimmerman, and A. C. Gossard, *Appl. Phys. Lett.* **104**, 211106 (2014).
- [59] T. T. Heikkilä, J. Särkkä, and F. K. Wilhelm, *Phys. Rev. B* **66**, 184513 (2002).
- [60] M. Chauvin, P. vom Stein, H. Pothier, P. Joyez, M. E. Huber, D. Esteve, and C. Urbina, *Phys. Rev. Lett.* **97**, 067006 (2006).
- [61] A. H. Dayem and C. C. Grimes, *Appl. Phys. Lett.* **9**, 47 (1966).

- [62] L. Bretheau, Ph.D. thesis, Ecole Polytechnique X, 2013.
- [63] J. Basset, M. Kuzmanović, P. Virtanen, T. T. Heikkilä, J. Estève, J. Gabelli, C. Strunk, and M. Aprili, *Phys. Rev. Res.* **1**, 032009(R) (2019).
- [64] J. Ridderbos, M. Brauns, A. Li, E. P. A. M. Bakkers, A. Brinkman, W. G. van der Wiel, and F. A. Zwanenburg, *Phys. Rev. Mater.* **3**, 084803 (2019).
- [65] R. L. Kautz and J. M. Martinis, *Phys. Rev. B* **42**, 9903 (1990).
- [66] PYTHON code for the RCSJ model is available at https://github.com/donfuge/rcsj_sde.
- [67] W. C. Stewart, *Appl. Phys. Lett.* **12**, 277 (1968).
- [68] P. Welch, *IEEE Trans. Audio Electroacoust.* **15**, 70 (1967).
- [69] <https://doi.org/10.5281/zenodo.7961884>.